Bulletin of the Seismological Society of America, Vol. 107, No. 3, pp. 1107–1117, June 2017, doi: 10.1785/0120160298

Ⓔ

The 2008 Wells, Nevada, Earthquake Sequence: Source Constraints Using Calibrated Multiple-Event Relocation and InSAR

by Jennifer L. Nealy, Harley M. Benz, Gavin P. Hayes, Eric A. Bergman, and William D. Barnhart

Abstract The 2008 Wells, Nevada, earthquake represents the largest domestic event in the contiguous United States outside of California since the October 1983 Borah Peak earthquake in southern Idaho. We present an improved catalog, magnitude complete to 1.6, of the foreshock–aftershock sequence, supplementing the current U.S. Geological Survey Preliminary Determination of Epicenters catalog with 1928 well-located events. To create this catalog, both subspace and kurtosis detectors are used to obtain an initial set of earthquakes and associated locations. The latter are then calibrated through the implementation of the hypocentroidal decomposition method and relocated using the Bayesloc relocation technique. We additionally perform a finite-fault slip analysis of the mainshock using Interferometric Synthetic Aperture Radar (InSAR) observations. By combining the relocated sequence with the finite-fault analysis, we show that the aftershocks occur primarily up-dip and along the southwestern edge of the zone of maximum slip. The aftershock locations illuminate areas of postmainshock strain increase; aftershock depths, ranging from 5 to 16 km, are consistent with InSAR imaging, which shows that the Wells earthquake was a buried source with no observable near-surface offset.

Electronic Supplement: Description of methods and figures of relocated aftershocks, interferograms, residuals, transformations, and seismic station locations.

Introduction

On 21 February 2008 at 14:16:02 (UTC), Wells, Nevada, experienced an M_w 6.0 earthquake, the largest event in the state within the past 50 years. The earthquake was felt throughout most of Nevada with shaking extending into Utah, Wyoming, and Oregon. Located beneath the historic town of Wells, the event injured three people and cost the community more than $10 million (dePolo *et al.*, 2011).

Despite the impact of the event, little work has been published that characterizes the mainshock and its subsequent aftershock sequence from a seismotectonic perspective. Although the slip distribution of the event has been analyzed (e.g., Dreger *et al.*, 2011) and earthquake relocations have been performed (e.g., Smith *et al.*, 2011), no studies have attempted to interpret such data together to better understand the kinematics of the earthquake sequence, the causative fault or faults, the relationship between surface deformation, mainshock slip, and aftershock locations, and the implications for seismic hazard in this region.

Here, we revisit the earthquake sequence using a variety of seismological and geodetic observations and modeling approaches (e.g., subspace detection, multiple-event relocation, and finite-fault modeling from Interferometric Synthetic Aperture Radar [InSAR]) to improve our understanding of the spatiotemporal variations of the foreshock–aftershock sequence. We use a combination of kurtosis and subspace detection and multiple-event relocation techniques to both significantly lower the magnitude of completeness and to improve knowledge of the absolute locations of events in the sequence (Harris, 2006; Baillard *et al.*, 2014). Using these tools and data from a combination of USArray Transportable Array (TA) stations, permanent monitoring stations in Nevada and Utah, and temporary stations deployed after the mainshock, we construct a relocated catalog of 1928 earthquakes located within ~250 km of the epicenter from February through August 2008.

We complement our modeling of the earthquake sequence locations by performing a finite-fault slip analysis of the mainshock from a suite of coseismic InSAR observations. Together, the InSAR observations and our sequence locations allow us to place the event in a seismotectonic context that reveals information about the causative fault and sequence kinematics at a level of detail that has not been available until now.

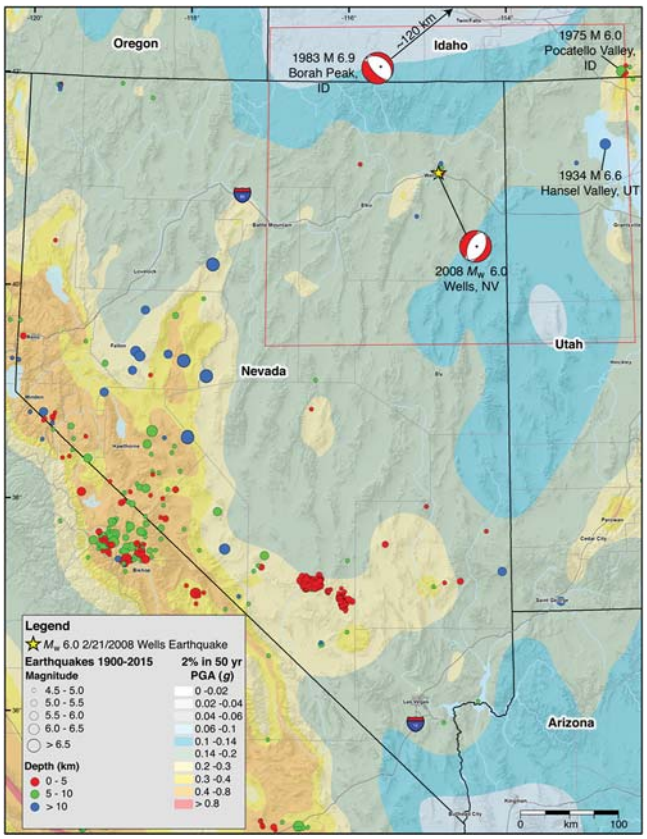

Figure 1. 2014 seismic-hazard map for the Nevada region. Historical events are represented by circles, sized by magnitude and colored by depth. The 2008 Wells, Nevada, earthquake is shown as a star with the focal mechanism for the event indicated below. The focal mechanism for the 1983 Borah Peak, Idaho, earthquake (located ~120 km from the north edge of the map) is also shown at the top of the map. The red bounding box indicates the region of interest for this study, shown in Figure 2.

Seismicity Monitoring and Seismicity in Northeastern Nevada

Historically, there have been relatively few moderate-to-large magnitude ($M_w > 6$) earthquakes in the region surrounding the M_w 6.0 Wells earthquake (Fig. 1), which is considered an area of relatively low seismic hazard within the broader Basin and Range Province (Petersen *et al.*, 2014). It is estimated that in northeastern Nevada, earthquakes of M_w 6 or larger can be expected with an occurrence rate of ~0.01 per year (i.e., one M_w 6 or larger event every 100 years; Anderson, 2011). Prior to the 2008 M_w 6.0 Wells sequence, seismicity in the area was generally diffuse and not concentrated on specific structures. Notable moderate-to-large events within 250 km of the Wells event include the 1934 M_w 6.6 Hansel Valley, Utah, earthquake and the 1975 M_w 6.1 Pocatello Valley, Idaho, earthquake (Arabasz *et al.*, 2016). Both of these events are inferred to have occurred on basin-bounding normal faults. The largest previous earthquake in northeastern Nevada was a 2001 M_w 4.6, approximately 43 km north of Elko (Fig. 2).

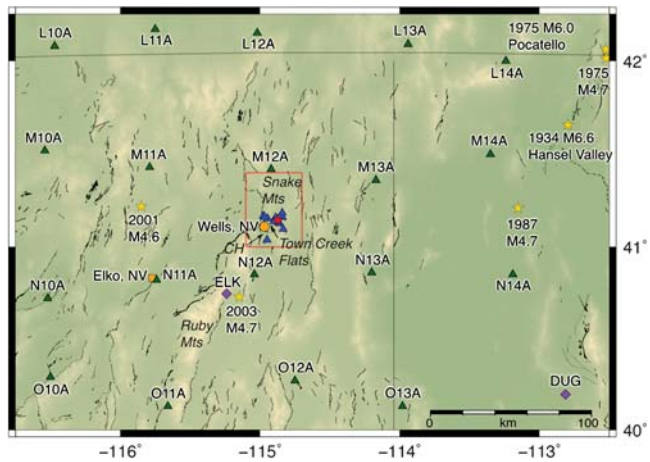

Figure 2. Location map of area around Wells, Nevada (octagon). The center star shows the location of the mainshock epicenter. Triangles mark locations of the EarthScope USArray Transportable Array stations, and diamonds indicate the permanent stations used in this study. Labeled stars show historical events in the region (M_w 4.5 and above), and the square shows the town of Elko. CH indicates the Clover Hill fault location.

The M_w 6.0 Wells earthquake occurred on a previously unmapped fault lying beneath the Town Creek Flats basin, which is located northeast of the Ruby Mountains and southeast of the Snake Mountains (Fig. 2). *W*-phase moment tensor modeling characterizes the earthquake as a normal fault occurring at a depth of 11.5 km with a strike, dip, and rake of 26°, 41°, and −97°, respectively, for one of the nodal planes (Hayes *et al.*, 2009). There is no reported evidence of the fault breaking the surface (Smith *et al.*, 2011), which is consistent with a published finite-fault model (Dreger *et al.*, 2011) that places the majority of slip between depths of 6 and 10 km with a maximum slip of ~1 m at a depth of ~7 km. The event was reported to have a long duration and comparatively high ground motion, features that are attributed to trapped seismic energy caused by thick sediments beneath the town of Wells (Biasi and Smith, 2011).

At the time of the earthquake, the U.S. Geological Survey (USGS) operated the two closest permanent stations: station ELK near Elko, Nevada, and station DUG near Dugway, Utah, ~40 and 200 km from the epicenter, respectively (Fig. 2). Fortuitously, the temporary EarthScope TA also surrounded the mainshock, with the closest station (M12A) ~30 km away. The close proximity of several TA stations to the earthquake sequence provides a unique opportunity to apply advanced detection methods to lower the detection threshold of the regional earthquake catalog and to compute minimally biased earthquake locations for the whole sequence. We use the closest 19 TA stations (L10–L14, M10–M14, N10–N14, and O10–O13) and permanent stations DUG and ELK, because this combination of stations provides excellent azimuth control on *Pg*, *Pn*, *Sg*, and *Sn* arrival-time observations to distances of ~250 km. Following the mainshock, both the University of Nevada, Reno, and the University of Utah

deployed temporary stations within the epicentral region. In our relocation procedures, arrival times from these stations are used to provide accurate depth control on a sufficient number of aftershocks from which we can, in turn, constrain the depth of the mainshock and larger aftershocks, as explained in greater detail below.

Previous Studies of the Wells Earthquake

Following the 2008 Wells sequence, several studies evaluated the geophysical setting of the event (Henry and Colgan, 2011; Ponce *et al.*, 2011; Ramelli and dePolo, 2011). These studies focused on determining what the Wells mainshock could contribute to current knowledge of faults in the surrounding area and how geophysical features may have played a role in the earthquake rupture. The research into the geophysical setting of the Wells event involved both field surveys of known faults near the epicenter, as well as the use of gravity and magnetic methods. Results indicated that the earthquake occurred on a northern strand of the Clover Hill fault that was previously unrecognized (Henry and Colgan, 2011) and that the proximity of the earthquake to the intersection of a basement gravity anomaly and a magnetic anomaly may have affected the regional stress regime that influenced the event (Ponce *et al.*, 2011).

The Nevada Bureau of Mines and Geology released two source studies of the sequence (Dreger *et al.*, 2011; Smith *et al.*, 2011). The first study analyzed the aftershock sequence and used a relative relocation method for locating aftershocks to reveal details of the aftershock distribution (Smith *et al.*, 2011). These relocations used the nearby temporary stations deployed by the University of Utah, the University of Nevada, Reno, and the USGS. However, because these stations were not in place prior to the mainshock, the first several days of the sequence, including many of the larger aftershocks, could not be relocated. The Smith *et al.* study concluded that the relocated aftershocks clearly defined the orientation of the mainshock fault plane. They also inferred that the area free of aftershocks within the central fault plane represents the extent of the coseismic rupture.

The second source study performed a finite-source analysis and a seismic moment tensor analysis for the Wells earthquake (Dreger *et al.*, 2011). This study analyzed a finite-source inversion using InSAR line-of-sight displacement results. Although the relocated aftershock sequence from the Smith *et al.* study was found to broadly agree with these finite-source results, they noted that there was a depth discrepancy between the geodetic and seismic models. This discrepancy was thought to result from a potential error in the hypocenter location upon which the fault-plane location in the inversion was based.

In this study, we are able to relocate the entirety of the sequence, including the mainshock and the initial 40 hrs of aftershocks that occurred prior to the deployment of the first temporary stations. We are also able to take advantage of our improved detection capabilities to supplement our catalog with hundreds of smaller events that had not been originally (routinely) detected. Using the newly produced well-calibrated earthquake catalog, we can compare our aftershock relocations with a fault-source solution generated from InSAR.

Seismic Event Detection and Automatic Processing

A catalog of foreshock and aftershocks related to the M_w 6.0 Wells, Nevada, earthquake was constructed by applying automated detection and arrival-time picking procedures designed to provide high-quality *Pg*, *Pn*, *Sg*, and *Sn* arrival times down to a relatively low-magnitude threshold. We chose a continuous correlation method described by Harris (2006) and implemented by Benz *et al.* (2015) that finds a minimum set of waveform templates (subspace) for each station that best represents the waveform variability of the foreshock–aftershock sequence. To further improve estimates of arrival times derived from the subspace detection process, we also used a kurtosis phase picker to refine our pick times, primarily for the more emergent *Pn* arrival times.

Subspace Detection

Generally, singular value decomposition of selected three-component waveforms that best represent an aftershock sequence results in a set of basis vectors whose linear combination can reconstruct the observed data. For well-behaved datasets, the number of basis vectors required to describe the observed data is sufficiently smaller than the number of observed waveforms. Consequently, constructing subspace detectors (waveform templates) reduces the problem to the fewest number of waveform templates needed to objectively detect events within an aftershock sequence.

A search of the USGS Preliminary Determination of Epicenters (PDE) catalog in the region surrounding Wells, Nevada, from 21 February 2008 to 30 August 2008 identifies 112 hypocenters associated with the sequence. Assuming these earthquakes represent the overall distribution of seismicity for the sequence, we manually picked first arriving *P* and *S* waves for each event at the closest 19 TA stations (picks for ELK and DUG were already in the PDE). These additional picks enabled us to window the TA station waveform data about either the *P* or *S* wave for construction of subspace detectors. We constructed three-component subspace detectors for each of the 19 TA stations and stations ELK and DUG using observed waveforms for the PDE events.

For a typical station in this study, we filtered the data between 1 and 4 Hz, selected a window containing either the *P* or *S* wave (ranging in size from 3 to 25 s), and aligned the waveforms on the appropriate phase. Closer stations had shorter time series, whereas more distant stations had longer time series. *P*-wave time-series lengths were typically from the onset of the *P* wave to the onset of the *S* wave, whereas *S*-wave time-series lengths were from the onset of the *S*-wave amplitude until the phase amplitude dropped to the background coda. Importantly, the lengths of the time series were

chosen to maximize the detection of true events, while minimizing false detections from a higher noise floor for short time series. The 1–4 Hz filter band represented the best tradeoff between enhancing the signal-to-noise ratio, while keeping the number of subspace waveforms needed to best represent the dataset low.

From a starting waveform dataset, typically composed of around 73 waveforms, we constructed 22 templates, on average, that were then used to form the subspace detector. The detector created from the templates was able to represent 90% of the input waveforms. For each station, the subspace detectors were run from 1 February to 31 August 2008. The templates used to generate the subspace detector are correlated with the observed data at the station of interest and a sufficient statistic (equivalent to the square of the correlation coefficient) is obtained. A z-score representing the number of standard deviations that a sufficient statistic is from, the mean is then computed and used to declare detections. Event detections were declared and P- or S-wave picks generated when the z-score exceeded a threshold of 6. We chose to use a z-score-based threshold rather than a threshold based on the sufficient statistics because the z-score takes into account the changing mean in each considered window, allowing a single threshold value to be selected for the entire dataset.

We found significantly fewer P-wave detections at distant stations primarily because of the emergent nature of the Pn and a higher degree of waveform variability for both Pg and Pn phases. Over the study period, 240,132 detections were made using the subspace detector with a maximum of 22,128 P arrival times and 23,348 S arrival times for the closest station, M12A.

Association of the P- and S-wave arrival times for all 21 stations resulted in a catalog of 2157 earthquakes between 1 February and 31 August 2008. The automated association, single event location, and determination of local (or Richter) magnitude (M_L) were performed using the National Earthquake Information Center processing system (Patton *et al.*, 2016). We found the resulting automatic catalog mostly reproduced the PDE catalog while significantly extending it to smaller magnitudes. Several PDE events were missing in the automatic processing; however, close inspection of their related data found smaller earthquakes preceding each missing event of interest, thus confusing the locator or estimate of magnitude. For those cases, the missing PDE events were created through a manual review process and added to the catalog.

Kurtosis Detector

To improve the P arrival times generated from subspace detection processing, we implement a kurtosis detector and picker (Baillard *et al.*, 2014) that was run against the same stations for the (shorter) time period of 20 February to 10 June 2008, which contained the majority of the aftershock sequence. Kurtosis detectors allow for automated P- and S-wave onset picking through the use of a modified kurtosis function, which characterizes the shape of the statistical distribution of the data; this technique is described in more detail in the Ⓔ Methods section in the electronic supplement to this article. Our kurtosis detector was tuned to improve the overall pick quality of the first arriving P waves, and in particular, emergent Pn at the more distant stations. In our implementation, the data were filtered between 1 and 4 Hz, matching the selected band-pass filter used in the subspace detector. The kurtosis detector could not distinguish between the onset of the P- and S-wave phases, but the 2-s sliding window, used to move over the observed data, primarily triggered on the first arriving P wave. The kurtosis picks were automatically added to the existing dataset, replacing existing correlation detector picks for each event.

Calibrated Multiple-Event Relocation

Automatic detection and association resulted in a catalog of 2157 earthquakes—magnitude complete to M_w 1.6. This represents a 20-fold increase in the number of events found in the USGS PDE. To ensure the computation of a minimally biased catalog of earthquake relocations, we manually reviewed all arrival times for the 986 events M_w 2 or larger. During this review, we also added P and S arrival times from four short-period University of Utah Seismograph Stations (UUSS) temporary stations that are within approximately two focal depths of many of the recorded aftershocks. These stations were not included in the automatic detection and picking process because of their short 4-week operational duration (March 2008) and limited dynamic range, making them more difficult for implementing automatic detectors and pickers that rely on continuous unclipped data. Nevertheless, their contribution was significant because they were the closest observing stations, thus enabling direct calibration of event epicenter, depths, and origin times for events recorded by two or more of the networks.

Calibration of Earthquake Locations Using Selected Earthquake Clusters

We chose to use hypocentroidal decomposition (HD; Jordan and Sverdrup, 1981) for calibration of the 986 manually reviewed events. The HD method (described in detail in the Ⓔ Methods section in the electronic supplement) separates the earthquake relocation problem into two components; a calibrated absolute location of the earthquake cluster and relative locations of the individual events in the cluster. Calibrating the cluster location leads to minimally biased relative locations of individual events. Minimally biased locations are important to place the hypocenter of the mainshock on a causative fault, if known, and to provide finer details of the seismotectonics and space–time evolution of the sequence from the relative aftershock relocations. The best absolute earthquake locations are obtained for a subset of earthquakes in the sequence that includes arrival-time data from the UUSS, TA, and/or USGS stations. These earthquakes are the least biased,

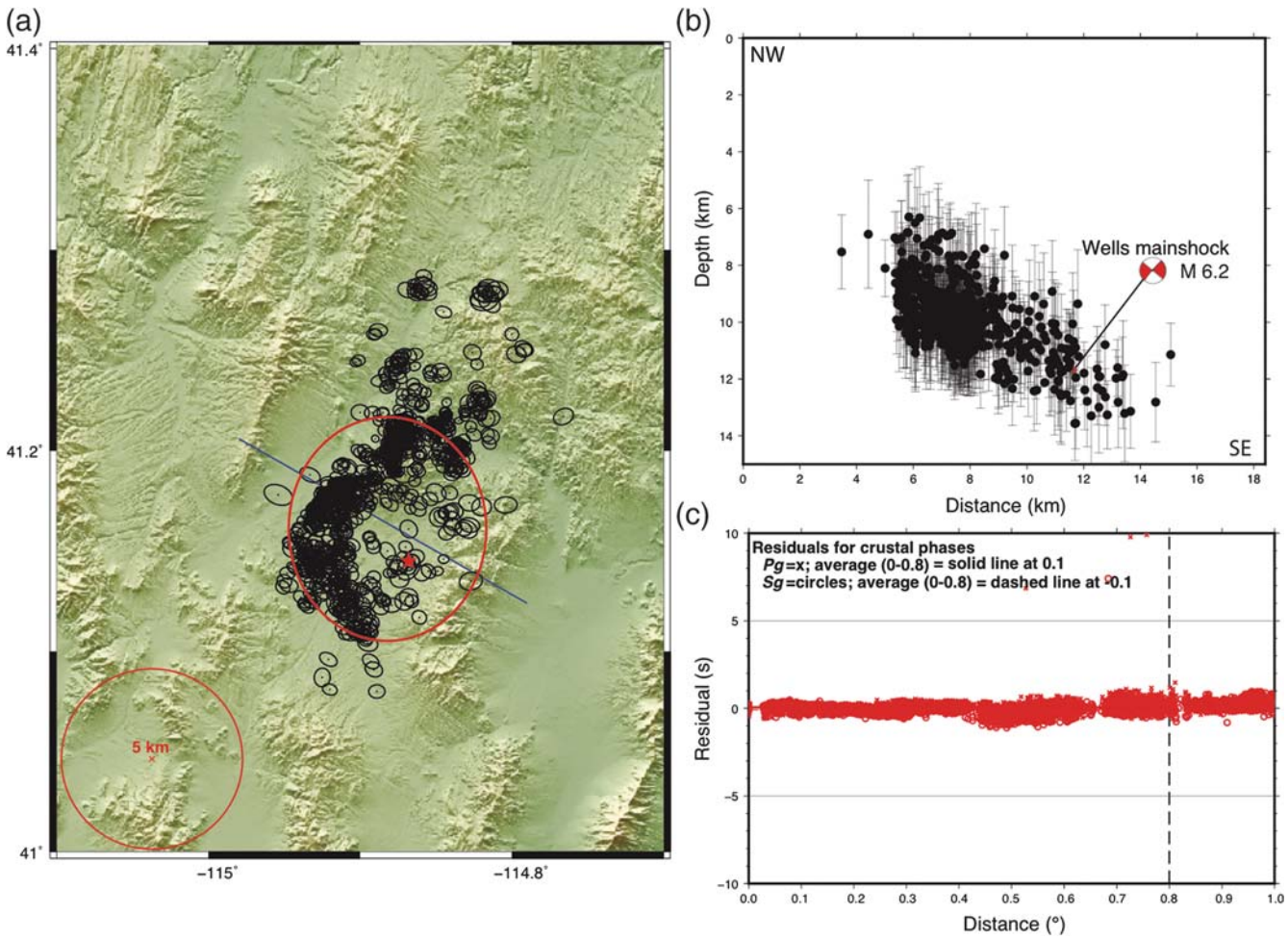

Figure 3. (a) The 986 calibrated events obtained from the hypocentroidal decomposition (HD) relocation technique. Events are represented by black dots and are surrounded by their corresponding 90% confidence ellipse. The line shows the location of the cross section, and the star represents the mainshock. The ellipse surrounding the mainshock shows the estimated region of nucleation based on Interferometric Synthetic Aperture Radar (InSAR) results. The circle in the lower left is a 5-km (radius) reference ellipse. (b) Cross section of the calibrated events showing the dip of the fault. (c) Plot of residuals for near-source readings used in the HD relocation technique. *Pg* readings are represented by ×, and *Sg* readings are represented by circles. The readings shown above a residual of 5 s are outliers and were not included in the final relocation run.

thus providing important constraints on foreshock, mainshock, and aftershock relocations. A modified version of the western United States (WUS) velocity model of Herrman *et al.* (2011) was used in computing travel times. Trial-and-error comparison between the *Pg*, *Sg*, *Pn*, and *Sn* travel-time curves and the HD estimates of travel times were used to adjust the velocity model. The hypocentroid of the manually reviewed earthquake clusters only uses arrival times observed to 0.8°, whereas arrival-time data to ~3° are used in determining the relative locations of each earthquake to the hypocentroid. For this sequence, the HD method was performed on nine clusters, each containing at least five common events to maintain connectivity.

The final HD relocations and travel-time fits for the 986 manually reviewed earthquakes are shown in Figure 3. A map view (Fig. 3a) of seismicity shows locations trending to the northeast, consistent with the *W*-phase nodal plane, with a formal average horizontal uncertainty of ±0.88 km. A northwest–southeast cross section through the seismicity (Fig. 3b) shows earthquakes occurring over a depth range of 6–14 km, with the mainshock occurring near the down-dip limit at a depth of 12 km. The average focal depth uncertainty is ±1.36 km. The formal uncertainty in the hypocentroid locations is 0.6–1.1 km at a 90% confidence level.

Multiple-Event Relocations of the Complete Catalog Using Calibrated Relocations as Priors

Earthquake relocation using the HD method is time consuming, making it difficult to determine the locations of the large number of earthquakes. Consequently, we used Bayesloc to compute multievent relocations for the entire dataset using the HD locations and error estimates as prior constraints in the Bayesian inversion. Precise relative relocations to lower magnitude thresholds can perhaps provide more

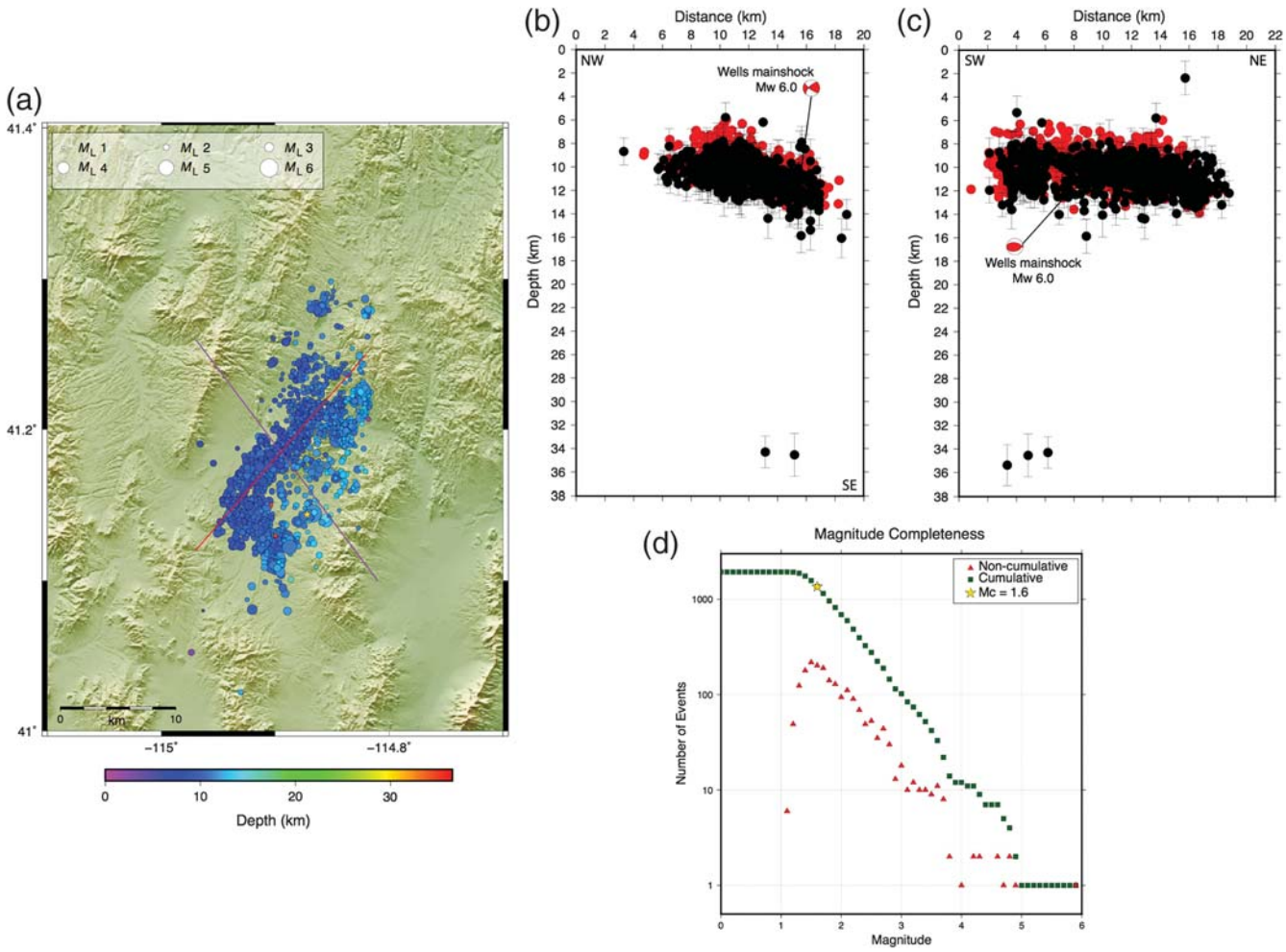

Figure 4. (a) The 1928 relocated events with hypocentroidal errors of less than 2 km. Events are represented by circles and colored by depth. The star indicates the mainshock location. (b) Cross section of the relocated events showing the dip of the fault. Red circles indicate events relocated with the HD technique and used as priors in the Bayesloc relocation. Black circles show events relocated using Bayesloc. (c) Vertical cross section of the relocated events along the strike of the fault. Red circles indicate events relocated with the HD technique and used as priors in the Bayesloc relocation. Black circles show events relocated using Bayesloc. (d) Magnitude completeness for the relocated catalog. Red triangles show the noncumulative magnitude curve, and green squares show the cumulative magnitude curve.

details on spatiotemporal variations in seismicity not revealed in a smaller catalog of larger magnitude events.

Bayesloc is a multiple-event relocation method that combines a travel-time model, an arrival-time measurement model, and an *a priori* statistical model (Myers *et al.*, 2007) in a joint probability formulation to relocate large sets of earthquakes. A Markov chain Monte Carlo approach can then be used to draw realizations from the joint posterior distribution, and the obtained samples can be used to estimate probability regions, epicenter locations, and parameter correlations. The samples can also be used to compute uncertainty estimates such as confidence bounds. The Bayesloc algorithm used within this study also determines *a posteriori* phase labels within the location procedure (Myers *et al.*, 2009, 2010).

To obtain relative locations for the ensemble catalog of 2157 earthquakes, we used 984 HD locations, excluding two older events, as priors in the Bayesloc relocations and the same modified WUS velocity model. Figure 4 shows the relocated seismicity for the complete catalog, which contained 1928 well-located events that had horizontal uncertainties within 2 km. The complete catalog has an average horizontal uncertainty of ± 1.15 km and depth uncertainty of ± 2.58 km, similar to that observed in the HD processing. The 1173 earthquakes smaller than M_w 2 provide no additional details on the overall pattern of aftershock seismicity when compared with the distribution of 986 HD-relocated events.

Finite-Fault Modeling/InSAR Analysis

We also investigate the finite-fault slip characteristics of the Wells earthquake, along with the spatial relationship between mainshock slip and subsequent aftershocks, using InSAR observations from the Envisat C-band and Advanced Land Observation Satellite (ALOS) Phased Array Type L-Band Synthetic Aperture Radar (PALSAR) L-band satellites (Table 1). InSAR observations provide complementary

Table 1
Details of InSAR Observations Used in This Study

Sat.	Path	Day 1 (yyyy/mm/dd)	Day 2 (yyyy/mm/dd)	Bperp (m)
Envisat	220	2007/11/14	2008/04/02	21
Envisat	399	2007/08/13	2008/04/13	356
Envisat	492	2007/04/02	2008/04/21	81
ALOS	207	2007/09/18	2008/05/05	2040

Sat. indicates the origin satellite; Path indicates the observations path/track number; Day 1 and Day 2 are the pre- and postevent acquisition dates, respectively; and Bperp is the perpendicular baseline (in meters) between the two acquisitions. InSAR, Interferometric Synthetic Aperture Radar.

information about the spatial distribution of subsurface fault slip. When available, well-located seismicity may be used to calibrate inversion of InSAR observations in which coseismic slip is blind and the responsible fault geometry and location are unknown. Here, we explore the degree to which inversions of blind fault slip may be improved by high-precision earthquake relocations.

We processed coseismic interferograms using the InSAR Scientific Computing Environment (ISCE; Agram *et al.*, 2013). We removed the topographic phase with the 30-m Shuttle Radar Topography Mission digital elevation model (Farr *et al.*, 2007) and unwrapped the interferometric phase through a two-step unwrapping procedure implemented in ISCE that uses the Statistical-cost Network-flow Approach for Phase Unwrapping (Chen and Zebker, 2001).

We inverted the resulting interferograms for fault slip following the general methodology of Barnhart and Lohman (2013) and Barnhart *et al.* (2015), assuming a homogeneous elastic half-space solution (Meade, 2007). First, we downsampled each interferogram to a computationally feasible number of observations ($\sim 10^3$ pixels per interferogram) and estimated the covariance structure of the resampled observations (Lohman and Simons, 2005; Lohman and Barnhart, 2010). Then, we conducted three suites of fault-slip inversions (Table 2). First, we derived the fault source model with no *a priori* location constraints from the relocated aftershock locations. We inverted the surface displacements for the best-fitting location (longitude, latitude, and depth) and orientation (strike, dip, and rake) of a single rectangular fault patch with uniform slip using the neighbourhood algorithm (Okada, 1992; Sambridge, 1999). In this inversion, we fixed the model search space to strikes of 0°–40° and dips of 10°–60° based on geometric information from the earthquake centroid moment tensor (CMT). Our preferred fault plane has a strike of 25° and a dip of 41° to the southeast (Table 2), identical to the geometry of the *W*-phase CMT, within uncertainty. We then fixed the location of this fault plane, extended its dimensions to both along-strike and down-dip, and iteratively discretized the fault plane while inverting for distributed slip (Barnhart and Lohman, 2010). This discretization process resamples the fault plane into variably sized triangles that reflect the model resolution afforded by the observations. We applied a Laplacian regularization constraint, with the regularization constant chosen using the ${}_jR_i$ method (Barnhart and Lohman, 2010). We further used the ${}_jR_i$ criterion to provide a metric for the goodness of fit of our fault-slip distributions (Barnhart and Lohman,2010). The ${}_jR_i$ criterion defines a good fit as that which minimizes the biases introduced into the slip distribution by observational noise (perturbation error) and regularization of the fault-slip inversion (regularization error). The ${}_jR_i$ criterion includes information about the length scales of spatially coherent noise in the interferograms; thus, ${}_jR_i$ provides a more robust assessment of data misfit in interferograms than do other common misfit metrics that assume observational noise is normally distributed (i.e., root mean square [rms] misfit).

The best-fit slip distribution of this first inversion scheme fits the resampled InSAR observations well (Ⓔ Fig. S1; model 1, Table 2) with M_w 6.09. The slip distribution images maximum slip of ~60 cm and encompasses a slip depth range of ~4–12 km (Ⓔ Fig. S1). The peak slip depth, which we use as a corollary to the event centroid, is ~3 km shallower than the depth range of peak aftershock activity (Ⓔ Fig. S1). Generally, this slip distribution delineates a region that is up-dip of the relocated aftershocks, though there is substantial depth overlap between the deeper portions of imaged slip and the aftershock relocations (Ⓔ Fig. S1). There is also a noticeable horizontal offset between the location of our best-fit fault plane and the relocated after-

Table 2
Details of Fault-Slip Distributions Assessed in This Study

Model Number	Strike	Dip	Longitude (°)	Latitude (°)	*Z* (km)	M_w	rms (cm)	Note
1	25	41	−114.88	41.15	7.4	6.08	4.87	NA solution
2	25	41	−114.88	41.16	11.5	6.15	4.85	NA solution shifted
3	20	35	−114.87	41.16	11.8	6.13	4.95	Aftershock fit
4	26	41	−114.87	41.14	7.9	6.2	X	USGS CMT

Model 1 was derived from the neighbourhood algorithm (NA) without any additional constraints. Model 2 is the same as model 1, but with the fault plane shifted to intersect the aftershock distribution. Model 3 is a plane fit to the relocated aftershock distribution. Model 4 is the U.S. Geological Survey (USGS) centroid moment tensor (CMT) solution, which is shown for reference. Strike, strike of the fault plane; Dip, dip of the fault plane; Lat/Lon/*Z*, the location and depth of the center of the fault-slip patch with the largest slip magnitude; M_w, inferred magnitude; rms, root mean square misfit between the InSAR observations and the best-fitting slip distribution of each model.

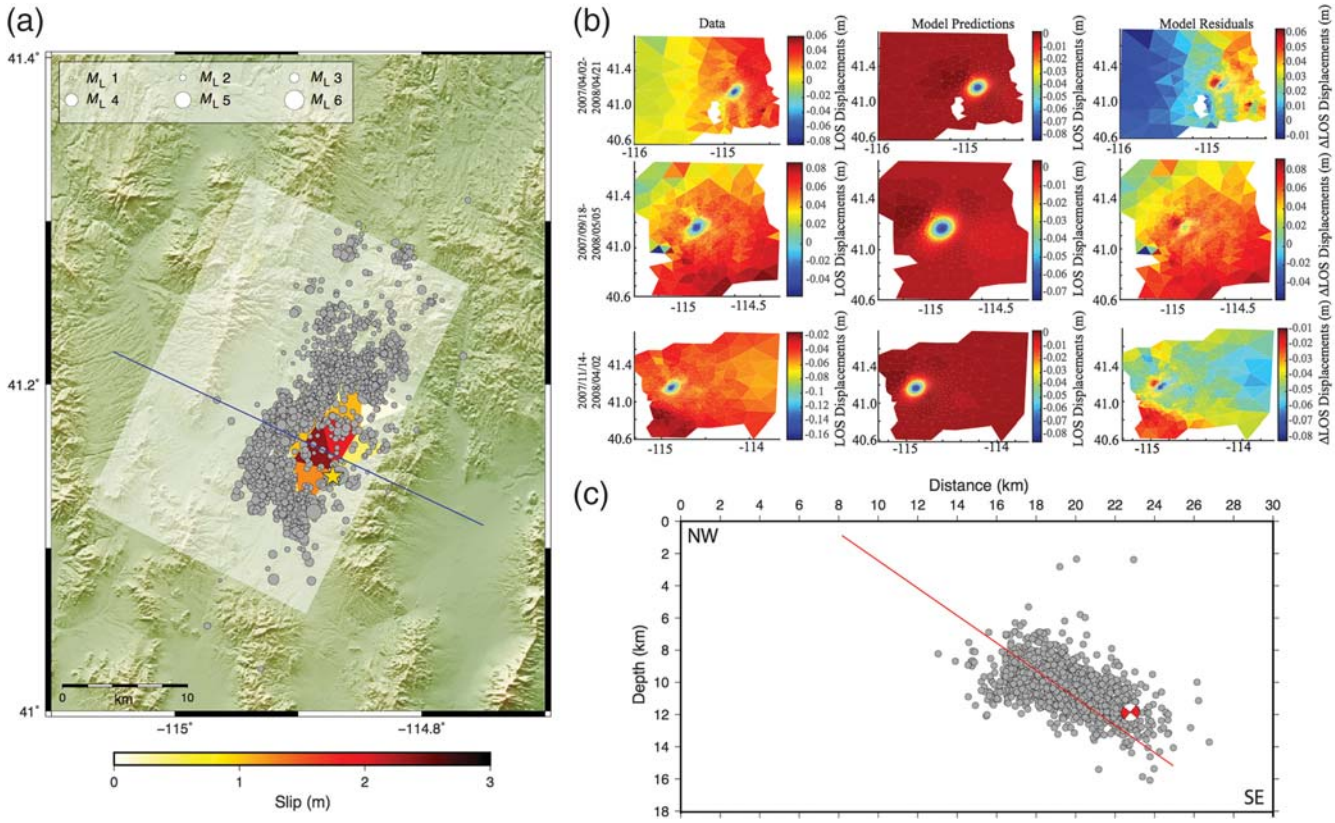

Figure 5. (a) Map view of the relocated aftershock locations with respect to slip distribution for the preferred inversion model (model 2). (b) Resampled interferograms, predicted displacements, and model residuals for InSAR model 2, described in Table 2. Resampled interferograms denoted by their acquisitions dates are detailed in Table 1. Line-of-sight (LOS) displacements are in meters, with negative displacements indicating line-of-sight increases (i.e., subsidence) and positive displacements indicating line-of-sight decreases (i.e., uplift). (c) Cross section along dip of the aftershock locations with respect to the slip distribution for the preferred inversion model. The line shows the location of the fault plane.

shocks, with the InSAR-estimated fault plane shifted 5–6 km southeastward of the relocated aftershock sequence. This spatial discrepancy implies that, if the InSAR-inferred fault plane and aftershock relocations are correct, then the aftershock sequence occurred within the footwall of the fault responsible for the mainshock. Because this scenario seems unlikely, we further explore the veracity of this offset.

To do so, we conduct a second inversion in which we shift the fault plane derived from the neighbourhood algorithm northwestward 5 km so that it is colocated with the band of seismicity (model 2, Table 2). Then, we apply the iterative distributed slip inversion described previously. In this inversion (Fig. 5), we find slip is shifted to depths of 9.5–14 km, whereas the surface projection of the slip distribution remains relatively unchanged from model 1. The model misfit as measured by rms misfit is virtually indistinguishable from model 1 (Table 2), though the presence of deeper slip requires greater slip magnitude to match the surface displacements (peak slip of ~2.4 m), which results in a higher estimated moment magnitude (M_w 6.15). In this iteration, imaged slip is primarily down-dip of the relocated aftershocks, with relocated aftershocks appearing to delineate the up-dip extent of imaged slip (Fig. 5a). Although the rms misfit of this model is lower than model 1, spatially coherent displacements are evident in model residuals that are more substantial than model 1 (Fig. 5b and Ⓔ Fig. S1). This suggests that the deeper fault slip does not provide a better fit to the surface displacements, though a simple quantitative measure of this is difficult to derive. The ${}_jR_i$ value of this fault-slip distribution is higher than that in model 1, suggesting that this model does not fit spatially coherent coseismic displacements as well (i.e., regularization error such that the displacements are underfit).

In our third inversion, we assume that the relocated aftershocks define the geometry of the rupture plane. We fit a plane to the relocated hypocenters, resulting in a fault plane with strike 20° and dip 35°, such that the fault plane is coplanar and colocated with the aftershock distribution (Ⓔ Fig. S2). We again apply the inversion for distributed slip as described above. The result of this inversion is similar to that of model 2, with slip concentrated down-dip of the aftershock sequence at depths of 9.5–14 km, and with larger slip values (M_w 6.13) necessary to fit the surface displacement pattern. As in model 2, the relocated aftershocks delineate

the up-dip bounds of the slip distribution. This model produces the largest rms misfit of the three models we test, yet the rms misfit is not demonstrably different from the other two models (Ⓔ Fig. S2; model 3, Table 2). Again, this fault-slip distribution leads to spatially coherent residuals that suggest the deeper and larger slip values do not fit the observations as well as shallower fault-slip source, as further evidenced by a higher ${}_jR_i$ value than in model 1.

Results

The earthquakes from the Bayesloc catalog were evaluated alongside the InSAR analysis to further validate the location of the aftershock sequence and slip distribution. From an InSAR-only perspective, model 1 would be the preferred model because it is the only model of the three explored that does not exhibit substantial coherent residual that is indicative of earthquake deformation (Fig. 5b and Ⓔ Figs. S1 and S2). InSAR-informed models 2 and 3 entail fault geometries that are better colocated with the aftershock sequence, but produce InSAR residuals that suggest real surface displacements are not fit as well as in model 1. To explore whether the calibrated earthquake locations could be relocated to better match the model 1 fault geometry and location, all of the events in the catalog were perturbed by ~5 km to the southeast. The residuals obtained for the shifted aftershock sequence have significantly more spread than the residuals from the original relocation and have a greater number of large residuals (Ⓔ Fig. S3). The increased spread and larger residuals following the shift indicate that the original relocations are a better fit for the sequence than the shifted locations.

The preference for the initial relocation over the shifted relocation seen in the residuals leads us to select model 2, which better fits the relocated aftershock distribution, as the preferred model for this study. The main slip calculated using this preferred InSAR model is located down-dip of the aftershocks and within the gap found between the southern and northern edges of the aftershock sequence. The depths of the relocated events and the dip of the sequence are also in agreement with the preferred InSAR model, with the geodetic fault plane lining up with the edge of the aftershocks (Fig. 5c).

The final catalog formed following the Bayesian multiple-event relocation is magnitude complete down to M_L 1.6. The locations of the events are comparable with those in the calibrated catalog with aftershocks extending 20 km along the strike of the fault, up-dip of the region of maximum slip, and along the southern edge of the maximum slip zone. A cross-section view of the relocated events indicates a southeast-dipping fault, which is in agreement with previous studies of this sequence and with the calibrated catalog. The calibrated catalog relocations show the majority of events have depths between 4 and 16 km. Based on the relocation errors obtained, as well as the depths of previously recorded earthquakes in this region, we believe that the locations of our calibrated catalog provide an accurate representation of the sequence, while also increasing the PDE catalog by 1814 well-located events, 877 of which were not previously contained in either the PDE or the Nevada network catalog.

Conclusions

By combining kurtosis and subspace detection techniques, thousands of events were identified in the months following the Wells mainshock as well as three foreshocks in the days leading up to the event. Multiple-event relocation resulted in a catalog of 1928 well-located events with a magnitude of completeness of M_w 1.6. The events in the new catalog provide a high degree of spatial and temporal resolution on the foreshock–aftershock sequence. Results show that the majority of aftershock seismicity takes place primarily up-dip and west of the mainshock slip and along the southwest edge of fault. Importantly, well-located aftershock seismicity is confined to a depth range of 5–16 km, consistent with the geodetic-derived slip model and lack of documented surface rupture (dePolo *et al.*, 2011).

When the relocated sequence is combined with our finite-fault analysis of the mainshock, we observe that the slip is primarily down-dip of the relocated aftershocks at depths of 9.5–14 km, with the majority of aftershocks delineating the up-dip extent of the slip. The foreshock–aftershock sequence extended for ~20 km along the strike of the fault and ~9 km along the southern edge of maximum slip. Overall, we find good agreement between our relocations and the preferred finite-fault model.

Finally, it should be noted that when comparing InSAR models, a straightforward best-fit approach to choosing a preferred slip distribution results in a fault geometry and location that is offset from the well-located aftershock sequence (model 1, Table 2). Perturbing this fault geometry to better align with the aftershock sequence results in a minimal change in fit, if not a better fit, when considering the rms misfit of the predicted surface displacements. However, rms misfit value does not capture spatially coherent surface displacements that are not fit by slip distributions optimized to fit the aftershock locations. This suggests that rms misfit is a particularly poor metric for assessing the fit of a model to data in the presence of spatially coherent displacement signals and noise, as is common in InSAR. Other metrics, such as the ${}_jR_i$ criterion, capture the fact that models 2 and 3 did not fit the surface displacement pattern nearly as well as model 1, despite equivalent or smaller rms values. It remains unclear in this particular sequence why the InSAR observations prefer a fault-slip distribution that is offset horizontally from the relocated sequence; possible causes may include our neglect of real Earth rigidity structure, unmodeled aseismic deformation, listric fault geometry, or other factors. This study indicates that it would behoove both the InSAR and seismic communities to further investigate the cause of such discrepancies to describe future sequences as accurately and congruently as possible.

Data and Resources

All data used in this article are available through the U.S. Geological Survey (USGS). Figures in this article were produced using the Generic Mapping Tools software package (Wessel and Smith, 1991). Either Gebco2014 bathymetry or a digital elevation model available through the USGS is used for basemaps (http://www.gebco.net, last accessed August 2016; http://nationalmap.gov/elevation.html, last accessed August 2016). Envisat imagery was acquired from the UNAVCO/WInSAR Synthetic Aperture Radar (SAR) archive; Advanced Land Observation Satellite (ALOS) Phased Array Type L-Band Synthetic Aperture Radar (PALSAR) imagery was acquired from the Alaska Satellite Facility. The catalog of relocated earthquakes for the 2008 Wells, Nevada, sequence is available in Science Base (doi: 10.5066/F7WS8RFK).

Acknowledgments

The authors would like to thank Will Yeck for his helpful insights into the multiple-event relocations and velocity models used. We would also like to thank the University of Nevada, Reno, for providing us with the most recent catalog of the Wells sequence from the Nevada Network to use for comparisons. Any use of trade, firm, or product names is for descriptive purposes only and does not imply endorsement by the U.S. Government.

References

Agram, P. S., R. Jolivet, B. Riel, Y. N. Lin, M. Simons, E. Hetland, and C. Lasserre (2013). New radar interferometric time series analysis toolbox released, *Eos Trans. AGU* **94,** no. 7, 69–70, doi: 10.1002/2013EO070001.

Anderson, J. G. (2011). Seismicity and seismic hazard of northeastern Nevada, *Nevada Bureau of Mines and Geology Special Publication 36*, 43–50.

Arabasz, W. J., J. C. Pechmann, and R. Burlacu (2016). A uniform moment magnitude earthquake catalog and background seismicity rates for the Wasatch Front and surrounding Utah region, *Earthquake Probabilities for the Wasatch Front region in Utah, Idaho, and Wyoming: Utah Geological Survey Miscellaneous Publication 16-3*.

Baillard, C., W. C. Crawford, V. Ballu, C. Hibert, and A. Mangeney (2014). An automatic kurtosis-based *P*- and *S*-phase picker designed for local seismic networks, *Bull. Seismol. Soc. Am.* **104,** no. 1, 394–409, doi: 10.1785/0120120347.

Barnhart, W. D., and R. B. Lohman (2010). Automated fault model discretization for inversions for coseismic slip distributions, *J. Geophys. Res.* **115,** no. B10, doi: 10.1029/2010JB007545.

Barnhart, W. D., and R. B. Lohman (2013). Phantom earthquakes and triggered aseismic creep: Vertical partitioning of strain during earthquake sequences in Iran, *Geophys. Res. Lett.* **40,** no. 5, 819–823, doi: 10.1002/grl.50201.

Barnhart, W. D., R. W. Briggs, N. G. Reitman, R. D. Gold, and G. P. Hayes (2015). Evidence for slip partitioning and bimodal slip behavior on a single fault: Surface slip characteristics of the 2013 M_w 7. 7 Balochistan, Pakistan earthquake, *Earth Planet. Sci. Lett.* **420,** 1–11, doi: 10.1016/j.epsl.2015.03.027.

Benz, H. M., N. D. McMahon, R. C. Aster, D. E. McNamara, and D. B. Harris (2015). Hundreds of earthquakes per day: The 2014 Guthrie, Oklahoma, earthquake sequence, *Seismol. Res. Lett.* **86,** no. 5, 1318–1325, doi: 10.1785/0220150019.

Biasi, G. P., and K. D. Smith (2011). *Final Technical Report USGS Cooperative Agreement for Seismic Network Operations*, Cooperative Agreement Award: 07HQAG0015, available at http://earthquake.usgs.gov/research/external/reports/07HQAG0015.pdf (last accessed August 2016).

Chen, C. W., and H. A. Zebker (2001). Two-dimensional phase unwrapping with use of statistical models for cost functions in nonlinear optimization, *J. Opt. Soc. Am.* **18,** no. 2, 338–351.

dePolo, C. M., K. D. Smith, and C. D. Henry (2011). Summary of the 2008 Wells, Nevada earthquake documentation volume, *The 21 February 2008 M_w 6.0 Wells, Nevada Earthquake: A Compendium of Earthquake-Related Investigations Prepared by the University of Nevada, Reno, Spec. Publ. 36*, 7–14.

Dreger, D. S., S. R. Ford, and I. Ryder (2011). Preliminary finite-source study of the February 21, 2008 Wells, Nevada earthquake, *Nevada Bureau of Mines and Geology Special Publication 36*, 147–156.

Farr, T. G., P. A. Rosen, E. Caro, R. Crippen, R. Duren, S. Hensley, and D. Seal (2007). The shuttle radar topography mission, *Rev. Geophys.* **45,** no. 2, doi: 10.1029/2005RG000183.

Harris, D. B. (2006). *Subspace Detectors: Theory*, United States Department of Energy.

Hayes, G. P., L. Rivera, and H. Kanamori (2009). Source inversion of the *W*-phase: Real-time implementation and extension to low magnitudes, *Seismol. Res. Lett.* **80,** no. 5, 817–822, doi: 10.1785/gssrl.80.5.817.

Henry, C. D., and J. P. Colgan (2011). The regional structural setting of the 2008 Wells earthquake and Town Creek Flat basin—Implications for the Wells earthquake fault and adjacent structures, *Nevada Bureau of Mines and Geology Special Publication 36*, 53–64.

Herrman, R. B., H. Benz, and C. J. Ammon (2011). Monitoring the earthquake source process in North America, *Bull. Seismol. Soc. Am.* **101,** 2609–2625, doi: 10.1785/0120110095.

Jordan, T. H., and K. A. Sverdrup (1981). Teleseismic location techniques and their application to earthquake clusters in the south-central Pacific, *Bull. Seismol. Soc. Am.* **71,** no. 4, 1105–1130.

Lohman, R. B., and W. D. Barnhart (2010). Evaluation of earthquake triggering during the 2005–2008 earthquake sequence on Qeshm Island, Iran, *J. Geophys. Res.* **115,** no. B12, doi: 10.1029/2010JB007710.

Lohman, R. B., and M. Simons (2005). Some thoughts on the use of InSAR data to constrain models of surface deformation: Noise structure and data downsampling, *Geochem. Geophys. Geosyst.* **6,** no. 1, doi: 10.1029/2004GC000841.

Meade, B. J. (2007). Algorithms for the calculation of exact displacements, strains, and stresses for triangular dislocation elements in a uniform elastic half space, *Comput. Geosci.* **33,** no. 8, 1064–1075, doi: 10.1016/j.cageo.2006.12.003.

Myers, S. C., G. Johannesson, and W. Hanley (2007). A Bayesian hierarchical method for multiple-event seismic location, *Geophys. J. Int.* **171,** no. 3, 1049–1063, doi: 10.1111/j.1365-246X.2007.03555.x.

Myers, S. C., G. Johannesson, and W. Hanley (2009). Incorporation of probabilistic seismic phase labels into a Bayesian multiple-event seismic locator, *Geophys. J. Int.* **177,** no. 1, 193–204, doi: 10.1111/j.1365-246X.2008.04070.x.

Myers, S. C., G. Johannesson, and N. A. Simmons (2010). *Bayesloc Multiple-Event Location Applied to a Global Data Set*, Lawrence Livermore National Laboratory, Livermore, California.

Okada, Y. (1992). Internal deformation due to shear and tensile faults in a half-space, *Bull. Seismol. Soc. Am.* **82,** no. 2, 1018–1040.

Patton, J. M., M. R. Guy, H. M. Benz, R. P. Buland, B. K. Erickson, and D. S. Kragness (2016). Hydra—The National Earthquake Information Center's 24/7 seismic monitoring, analysis, catalog production, quality analysis, and special studies tool suite, *U.S. Geol. Surv. Open-File Rept. 2016-1128*, 28 p., doi: 10.3133/ofr20161128.

Petersen, M. D., M. P. Moschetti, P. M. Powers, C. S. Mueller, K. M. Haller, A. D. Frankel, Y. Zeng, S. Rezaeian, S. C. Harmsen, O. S. Boyd, *et al.* (2014). Documentation for the 2014 update of the United States national seismic hazard maps, *U.S. Geol. Surv. Open-File Rept. 2014-1091*, 243 p., doi: 10.3133/ofr20141091.

Ponce, D. A., J. T. Watt, and C. Bouligand (2011). Geophysical setting of the February 21, 2008 M_w 6.0 Wells earthquake, Nevada, implications for earthquake hazards, *Nevada Bureau of Mines and Geology Special Publication 36*, 89–100.

Ramelli, A. R., and C. M. dePolo (2011). Quaternary faults in the 2008 Wells earthquake area, *Nevada Bureau of Mines and Geology Special Publication 36*, 79–88.

Sambridge, M. (1999). Geophysical inversion with a Neighbourhood Algorithm—II. Appraising the ensemble, *Geophys. J. Int.* **138,** no. 3, 727–746, doi: 10.1046/j.1365-246x.1999.00900.x.

Smith, K., J. Pechmann, M. Meremonte, and K. Pankow (2011). Preliminary analysis of the M_w 6.0 Wells, Nevada, earthquake sequence, *Nevada Bureau of Mines and Geology Special Publication 36*, 127–145.

Wessel, P., and W. H. Smith (1991). Free software helps map and display data, *Eos Trans. AGU* **72,** no. 41, 441–446, doi: 10.1029/90EO00319.

U.S. Geological Survey
National Earthquake Information Center
1711 Illinois Street
Golden, Colorado 80401
jnealy@usgs.gov
benz@usgs.gov
ghayes@usgs.gov
(J.L.N., H.M.B., G.P.H.)

Global Seismological Services
Golden, Colorado 80401
bergman@seismo.com
(E.A.B.)

Department of Earth and Environmental Sciences
University of Iowa
Iowa City, Iowa 52242
william-barnhart-1@uiowa.edu
(W.D.B.)

Manuscript received 28 September 2016;
Published Online 14 March 2017